

Inversion based on simultaneous observations of voltage and calcium concentration in iPSC-CMs

J.E. Jansen

Supervisors: Aslak Tveito (Simula Research Laboratory, Oslo),
and Patrick Farrell (Mathematical Institute, Oxford)

July 7, 2017

Abstract

We investigate the possibilities of parameter estimation of human induced pluripotent stem cell-derived cardiomyocytes (iPSC-CMs), based on data obtained by optical mapping, an alternative to the golden standard patch clamping technique. We will both look at parameter estimation based on single cell voltage and calcium measurements and at parameter estimation based on larger tissue measurements. We use the monodomain model and Paci2013 cell model for our simulations. We mainly investigate the estimation of the conductance parameters of the fast sodium current I_{Na} , the L-type calcium current I_{CaL} , the inward rectifier current I_{K1} and the rapid delayed rectifier current I_{Kr} . We define cost functionals \mathcal{J} and find minima for those four parameters. We also consider ion channel blocking and adjoint based optimization. We conclude that inversion based on optical mapping might be possible to use in the future, when both optical mapping recording techniques and iPS-CM monolayer production are further improved.

1 Introduction

We investigate an inverse problem based on simultaneous observations of voltage and intracellular calcium concentration. Mathematically, inversion means the computation of the most plausible values of not directly observable parameters using a set of measurements. The classic technique to estimate electrophysiological cardiac parameters is patch clamping. With patch clamping, the transmembrane voltage of a single cell can be precisely measured over time. An alternative for the time and labour intensive patch clamping technique could be optical mapping, with which voltage and calcium waves of a cluster of cells can be measured simultaneously [11].

The monodomain model is a commonly used model to simulate cardiac electro-physiology. We will investigate if we can use the monodomain model

to infer parameters based on voltage and intracellular calcium measurements. We will also try to infer model parameters using single cell measurements and will compare the results of both approaches. As a motivating example, we will model the behaviour of monolayers of human induced pluripotent stem cell-derived cardiomyocytes (iPSC-CMs), using the Paci2013 cell model. In recent years, there has been a large interest in iPSC-CMs as a tool for drug screening and disease modelling and more efficient techniques for doing so are needed.

1.1 Human induced pluripotent stem cell-derived cardiomyocytes (iPSC-CMs)

Stem cells are cells that can be developed into other cell types, such as cardiomyocytes (heart cells), hepatocytes (liver cells) and neurons (brain cells). There exist two types of human stem cells: embryonic and adult stem cells. A newly formed embryo consists for a large part of embryonic stem cells, that differentiate to form different parts of the body. After embryonic development, the body still contains stem cells: the adult stem cells. These can be found in different tissues and play a role in tissue repair. Normally, when a stem cell has differentiated into a somatic cell, such as a heart, liver, brain or skin cell, it can not change into another cell type anymore. However, since 2007, it has become possible to reprogram differentiated adult cells (somatic cells), such as skin cells, to become so called human induced pluripotent stem cells [26]. Such reprogrammed stem cells can then be differentiated into other cell types, such as the heart cells we are interested in. We call those heart cells human induced pluripotent stem cell-derived cardiomyocytes (iPSC-CMs). There has been a large interest in using iPSC-CMs for drug safety screening and disease modelling [21]. Human iPSCs are self-renewing, patient-specific, and provide a promising platform for studying cardiac cells *in vitro* [18]. In recent years, the techniques for efficiently producing homogeneous populations of iPSC-CMs have greatly improved. However, the production process of iPSC-CMs is still very expensive in comparison to most *in vitro* models. The largest limitation of the currently produced iPSC-CMs is their immature, and heterogeneous phenotype: the grown iPSC-CMs are typically a mix of ventricular-, atrial-, and nodal-like cells, although improvements in maturity and homogeneity are still being made [7].

1.2 Optical mapping

There are several techniques to study the electrophysiology of iPSC-CMs. The method most commonly used is whole-cell patch clamping. With this technique, a glass pipette electrode is inserted in the interior of a cell, creating a hole in the cell membrane. Then, the membrane potential of the cell can be controlled by applying voltage to the electrode. A resting cell membrane has a transmembrane potential of approximately -80 mV. Different types of ion channels open and close at different membrane potential values. When an ion channel is open, ions will flow through it, which results in a current. By controlling the voltage

and measuring the resulting current, information about the distribution and behaviour of the ion channels in the cell membrane can be gathered [20].

The measurements obtained in this way are very accurate, but patch clamping is time and labour intensive, and thus precludes efficient large-scale screening. An alternative to patch clamping is optical mapping, using voltage-sensitive dyes (VSDs) or genetically-encoded voltage indicators (GEVIs) [7]. Typically, a small point stimulus is applied somewhere in a patch of cells, after which the transmembrane potential is recorded with a camera. With optical mapping, the transmembrane potential v can be measured with a high spatial and temporal resolution. Unlike the invasive patch clamping technique, optical mapping allows for action potential measurements of large cell populations and sequential measurements of the same groups of cells for a longer period of time. Furthermore, it is possible to not only measure the transmembrane potential, but also the intracellular calcium concentration $[Ca]_i$, simultaneously [11]. Although optical mapping methods do not produce action potential measurements that are equivalent to the golden standard patch clamp measurements, recent proof-of-principle studies have shown that they might be similar enough to be used for disease modelling and drug testing [23]. In [6], for example, simultaneous measurements of voltage and calcium with the genetically encoded calcium and voltage reporter CaViar were used to screen for the cardiotoxicity of drugs. Further, in [5], a cardiac subtype specific GEVI was used, thus allowing for screening of only atrial-, ventricular- or nodal-like cells. However, those studies do not take in account the spatial resolution that optical mapping allows for. We will investigate what extra information those multiple cell measurements, such as the ≥ 1 cm large- diameter iPSC-CMs monolayer simultaneous voltage and calcium recordings from [11], can give us.

1.3 Overview

We introduce the classic monodomain equations in Section 2.1 and the Paci2013 cell model in Section 2.2. The Paci2013 cell model is specifically developed for the simulation of iPSC-CMs action potentials and is based on data obtained on iPSC-CMs [15, 14]. Due to the already mentioned immature phenotype of currently produced iPSC-CMs, the variability in the action potential shape of different cells is large, even if they are part of the same cell cluster [4, 28]. Therefore, the predictive value of the Paci2013 and other cell models will be limited and our investigation must be seen as a proof of concept. The development of iPSC-CMs technologies is rapid and it is hoped that future iPSC-CMs will be more homogeneous and similar to mature cardiomyocytes [7]. Sections 2.3-2.6 discuss the used software, numerical approximation, the inverse problem and input data. In Chapter 3, we describe our results, which are discussed in Chapter 4. We will look at the sensitivity of our measurements to the conductance parameters of several ion currents. Further, we define cost functionals \mathcal{J} and look for minima for the conductance paramters g_{Na} , g_{CaL} , g_{K1} and g_{Kr} . We also consider ion channel blocking and adjoint based optimization. We end with a conclusion, in which we discuss future directions.

2 Methods

2.1 The monodomain model

The monodomain equations are given by

$$\frac{\partial \mathbf{s}}{\partial t} = \mathbf{F}(\mathbf{s}, v), \quad \mathbf{x} \in H, \quad (1)$$

$$\frac{\partial v}{\partial t} + I_{\text{ion}}(v, \mathbf{s}) = \nabla \cdot (\mathbf{M} \nabla v) + I_s, \quad \mathbf{x} \in H, \quad (2)$$

$$\mathbf{n} \cdot (\mathbf{M} \nabla v) = 0, \quad \mathbf{x} \in \delta H, \quad (3)$$

with $v(\mathbf{x}, t)$ the transmembrane potential (in mV), H the domain, δH the boundary of H , \mathbf{n} the outward pointing normal of the boundary, I_s the prescribed input current (in mV/ms) and I_{ion} the ionic current across the membrane (in mV/ms), both scaled by the cell membrane capacitance (in $\mu\text{F}/(\text{mm}^2)$). Equation (1) is a system of ODEs that models the membrane dynamics. There exist many different cell membrane dynamics models with varying degrees of complexity that can be used to specify I_{ion} , $\mathbf{F}(\mathbf{s}, v)$, and the state variables \mathbf{s} . See the CellML repository [12] for an overview of different types of models. In this report, we will use the Paci2013 cell model that is specifically developed to model the electrophysical behaviour of iPSC-CMs [15]. We will introduce the Paci2013 cell model in the next section.

The conductivity tensor \mathbf{M} (in mm^2/ms) satisfies

$$\mathbf{M} = \frac{\alpha}{1 + \alpha} \mathbf{M}_i, \quad (4)$$

with $\mathbf{M}_e = \alpha \mathbf{M}_i$. Here, \mathbf{M}_e and \mathbf{M}_i are the extracellular and intracellular conductivities (in mm^2/ms), divided by the product of the membrane capacitance (in $\mu\text{F}/(\text{mm}^2)$) and the cell membrane area-to-volume ratio (in $1/\text{mm}$). By assuming that there exists an $\alpha \in \mathbb{R}$ such that $\mathbf{M}_e = \alpha \mathbf{M}_i$ the monodomain equations can be derived from the more complicated bidomain equations [10, p. 566-568].

2.2 The Paci2013 cell model

The Paci2013 model consists of 18 ODEs and is of Hodgkin-Huxley type (see [10, p.195-215] for an introduction to the Hodgkin-Huxley equations). The ionic current I_{ion} is a sum of twelve different ion channel type currents:

$$I_{\text{ion}} = I_{\text{Na}} + I_{\text{CaL}} + I_f + I_{\text{K1}} + I_{\text{Kr}} + I_{\text{Ks}} + \dots \quad (5)$$

$$I_{\text{to}} + I_{\text{NaCa}} + I_{\text{NaK}} + I_{\text{pCa}} + I_{\text{bNa}} + I_{\text{bCa}}. \quad (6)$$

Here, I_{Na} is the fast sodium current, I_{CaL} the L-type calcium current, I_f the hyperpolarization-activated cyclic nucleotide-gated ‘funny’ (pacemaker) current, I_{K1} the inward rectifier current, I_{Kr} the rapid delayed rectifier current, I_{Ks} the slow delayed rectifier current, I_{to} the transient outward current, I_{NaCa} the

sodium calcium exchanger, I_{NaK} the sodium potassium pump, I_{pCa} the sarcolemmal calcium pump current, and I_{bNa} and I_{bCa} are background currents. An ion channel current I_k is typically of the form

$$I_k = g_k m_k^{p_k} \dots h_k^{q_k} (u_m - u_k), \quad (7)$$

where g_k is the maximum conductance g_k (in $\mu\text{S}/\mu\text{m}^2$), u_k (in mV) the Nernst potential and $m_k, h_k \dots$ are a certain number of voltage and time dependent gating variables. Each ion channel type has different types and/or numbers of gating variables. The Paci2013 model contains ODEs to describe the dynamics of thirteen different ionic gating variable types. Apart from the ionic gating variables and an inner calcium dynamics gating variable, the state variables of the Paci2013 model include the intracellular sodium and calcium, and the sarcoplasmic reticulum calcium concentrations $[\text{Na}]_i$, $[\text{Ca}]_i$ and $[\text{Ca}]_{\text{SR}}$ [15]. We assume we can only measure the intracellular calcium concentration. This concentration rises in response to an action potential. The values of the default Paci2013 model parameters are mainly based on patch clamp iPSC-CM data from [14]. The iPSC-CMs studied in [14] showed atrial-, nodal-, and ventricular-like action potentials. The Paci2013 model contains two sets of parameters: one to simulate ventricular-like cells and one to simulate atrial-like cells. Without a stimulus, both the atrial and ventricular Paci2013 models beat spontaneously. We did not investigate this spontaneous beating, but applied a 1 Hz stimulus instead, as we assumed that this would produce more useful measurements in practice. Further, we only investigated the ventricular model. We choose the ventricular model over the atrial model because ventricular cells are more common than atrial cells and also the ones mainly used for drug tests [16].

2.3 Software

We used the `SingleCellSolver` module for all single cell simulations and the `splittingsolver` module for all tissue simulations. Both modules are part of the Python package [19]. This electrophysiology solver package is based on the FEniCS Project software [13] and the dolfin-adjoint software [8]. We retrieved the code for the Paci2013 cell models from the CellML repository: <http://models.cellml.org/e/16d/>. With a few minor adjustments¹, we could convert the models to working cbcbeat versions. The optimization problem is solved with the IPOPT open-source optimisation algorithm [27]. Our full code is available to download from https://github.com/JoannekeJansen/SABS_first_project.

¹The modifications were: the addition of necessary parentheses, the fixing of integer division, the renaming of the membrane potential, the removal of the inbuilt stimulus, and the adjustment of the expression for the gating variable m_∞ . The expression for the m_∞ variable had partly disappeared after the model was converted with the cbcbeat conversion script `gotran2beat`.

2.4 Numerical approximation

To solve the single cell Paci2013 ODE system, we used a first order generalized Rush-Larsen (GRL1) scheme [24]. To solve the monodomain PDE system and its coupled cell membrane dynamics ODE system, we used a first order Godunov splitting scheme. With an operator splitting scheme, the linear PDE system and nonlinear ODE system are solved separately, after which the solutions can be combined to form an approximate solution of the full system of equations [25]. After experimenting with different time step and mesh sizes and a first and higher order splitting scheme, the first order scheme turned out to be the fastest converging option. The nonlinear ODEs are solved again with a first order generalized Rush-Larsen scheme [24]. The PDE system is solved with continuous Galerkin piecewise linear finite elements in space and a theta-scheme discretization, with $\theta = 0.5$, in time. The theta-scheme with $\theta = 0.5$ was the default temporal scheme. We note that we could have used a faster first order backward Euler scheme ($\theta = 1$), as our temporal convergence is only first order due to splitting. We use the conjugate gradient (CG) method with PETSc algebraic multigrid preconditioner to solve the discretized PDE system [1, 2].

2.5 The inverse problem

With optical mapping techniques, it is possible to obtain measurements $[Ca]_i \text{ obs}$ of the intracellular calcium concentration and measurements v_{obs} of the transmembrane potential at discrete points in time. With those measurements, we want to estimate the value of certain parameters $\mathbf{c} \subseteq \{g_{\text{Na}}, g_{\text{CaL}}, g_{\text{Kr}}, g_{\text{K1}}, \dots\}$. For our single cell measurements, we formulate our optimisation problem as follows: find $\mathbf{c} \subseteq \{g_{\text{Na}}, g_{\text{CaL}}, g_{\text{Kr}}, g_{\text{K1}}, \dots\}$, such that the functional

$$\mathcal{J}_{\text{single cell}}([Ca]_i, v, \mathbf{c}) = \frac{1}{N} \underbrace{\sum_{i=1}^N \frac{\|[Ca]_i - [Ca]_i \text{ obs}(t_i)\|^2}{\|[Ca]_i \text{ obs}(t_i)\|^2}}_{\text{Left side}} + \underbrace{\frac{\|v - v_{\text{obs}}(t_i)\|^2}{\|v_{\text{obs}}(t_i)\|^2}}_{\text{Right side}}, \quad (8)$$

is minimized, subject to the requirements that $[Ca]_i, v$ and \mathbf{c} satisfy the state system of ODEs (1), initial conditions $v(\mathbf{x}, 0) = v_0(\mathbf{x})$ and $\mathbf{s}(\mathbf{x}, 0) = \mathbf{s}_0(\mathbf{x})$, and all parameters $g_{\text{Na}}, g_{\text{CaL}}, g_{\text{Kr}}, g_{\text{K1}}, \dots$ lie between 50% and 150% of their default values. Here, N are the number of measurements in time and $t_i, i = 1, \dots, N$ the respective moments in time. As we will only consider optimisation for a few parameters, we will not consider regularisation. We note that in a realistic problem with a spatially varying parameter field, i.e. with a very large number of parameters, the use of regularisation would be essential. We will refer to the contribution of the $[Ca]_i$ and v measurements as the left and right side of $\mathcal{J}_{\text{single cell}}$ respectively.

In a similar way, for the tissue measurements, we formulate our optimisation

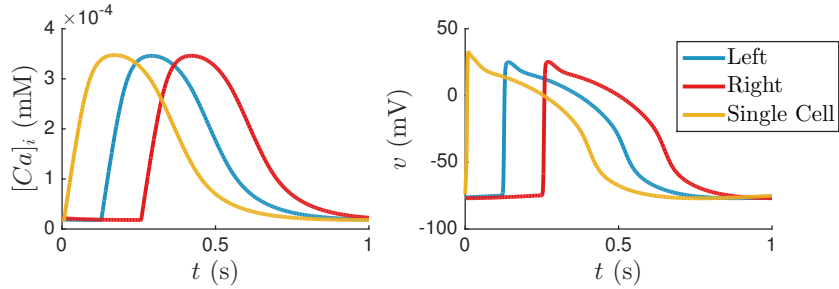


Figure 1: Plot of $[Ca]_i$ and v against t , at the left of the domain (in blue, at (5 mm, 0 mm)), at the right of the domain (in red, at (10 mm, 0 mm)) and for a single cell measurement (in yellow).

problem as follows: find $\mathbf{c} \subseteq \{g_{Na}, g_{CaL}, g_{Kr}, g_{K1}, \dots\}$, such that the functional

$$\mathcal{J}([Ca]_i, v, \mathbf{c}) = \frac{1}{N} \sum_{i=1}^N \underbrace{\frac{\|[Ca]_i - [Ca]_{i \text{ obs}}(t_i)\|_{L^2}^2}{\|[Ca]_{i \text{ obs}}(t_i)\|_{L^2}^2}}_{\text{Left side}} + \underbrace{\frac{\|v - v_{\text{obs}}(t_i)\|_{L^2}^2}{\|v_{\text{obs}}(t_i)\|_{L^2}^2}}_{\text{Right side}}, \quad (9)$$

is minimized, subject to the requirements that $[Ca]_i, v$ and \mathbf{c} satisfy the state system of equations (1)-(3), initial conditions $v(\mathbf{x}, 0) = v_0(\mathbf{x})$ and $\mathbf{s}(\mathbf{x}, 0) = \mathbf{s}_0(\mathbf{x})$, and all parameters $g_{Na}, g_{CaL}, g_{Kr}, g_{K1}, \dots$ lie between 50% and 150% of their default values. Again, N are the number of measurements in time and t_i , $i = 1, \dots, N$ the respective moments in time.

2.6 The input data

We generated synthetic observed single cell and tissue measurements. For the tissue case, we solved the system on a rectangular test domain of 12 mm \times 0.01 mm. We took time steps of 0.1 ms and a triangular mesh consisting of 200 by 1 cells (400 triangles). We took typical values $\sigma_t = 0.02$ and $\sigma_l = 0.2$ (in mS/mm) for the tangential and longitudinal conductivity respectively [22], data from [17, 3]. In the ventricular Paci2013 model, the total cell capacitance is $C_m = 9.87109 \times 10^{-5}$ (in μF). Further, we assumed that the total cell volume is a sum of the intracellular, 8800.00 (in μm^3), and SR, 583.73 (in μm^3), compartment volumes, as defined in the ventricular Paci2013 model. We ran the model in both cases for 800 s to reach a steady state, while applying a 1 Hz stimulus of 5 ms and 5.6 A/F, the default stimulus values of the Paci2013 ventricular model. For the tissue case, we applied the stimulus over the left 0.5 mm of the domain. We recorded and saved the values of v and $[Ca]_i$ every ms from $t = 0$ to $t = 1000$ ms. For the tissue case, we saved those values at all points in our domain. In [11], 926 optical mapping recordings per second were made with a 128×128 pixel camera. Therefore, it seems reasonable to assume we can record the voltage and calcium concentration every ms. We assume that the accuracy

and spatial resolution of our synthetic observed data is equal to our numerical solution at every recorded moment in time. In reality, the obtained data will be rounded to discrete values and averaged in space. Both the accuracy and spatial resolution of real data might be less than that of our synthetic data. In Figure 1, we plot both two points of the observed tissue data (in blue, at (5 mm, 0 mm) and in red, at (10 mm, 0 mm)), and the observed single cell data (in yellow), over time. We see that the calcium concentration peaks approximately 140 ms after the voltage does.

3 Results

3.1 Single cell computations

We are interested in the maximal conductance parameters of the main ion channel types: g_{Na} , g_{CaL} , g_{Kr} , g_{K1} , g_{Ks} , g_f and g_{to} . We assume that an increase or decrease in the standard values of the maximal conductance parameter of a specific ion channel type indicates an increase or decrease in the number of ion channels of that type expressed in the cell membrane. We investigated the sensitivity of our single cell data to the maximal conductance parameters by setting them in turn to 50% and 150% of their original values. In Figures 2 and 3, we show the results. Further, in Figures 4 and 5, we show several characteristics of our measurements: for both $[\text{Ca}]_i$ and v , we calculated the amplitude, the maximum upstroke velocity V_{\max} , and the time the measured concentration or potential was above 30%, 50%, 70% and 90% of its amplitude. We see that varying g_{Ks} , g_f or g_{to} has almost no visible effect on our measurements. We will interpret Figures 2-5 in our discussion.

3.2 Tissue computations

We investigated the sensitivity of our tissue data to the same parameters, and also to the conductivity parameter σ_t . We made similar plots as before, which we included in the Appendix, Figures 19-22. In Figure 21, we included a comparison of the conductance velocity through the tissue. For the calculation of all characteristics except the conductance velocity, we only used the measurements at the single point (5 mm, 0 mm), as the action potential and calcium concentration wave have approximately the same shape at all points. As before, we see that varying g_{Ks} , g_f or g_{to} has almost no visible effect on our measurements. In Figures 6-10, we show heat maps of v and $[\text{Ca}]_i$ at $t = 150$ ms after we started our recordings. In each Figure, we set one of the parameters g_{Na} , g_{CaL} , g_{K1} , g_{Kr} or σ_t to 50%, 75%, 100%, 125% and 150% of its default value. Again, we will interpret Figures 6-10 and Figures 19-22 in our discussion.

3.3 Inversion

We calculated the value of $\mathcal{J}_{\text{single cell}}$ and \mathcal{J} while varying one of the parameters g_{Na} , g_{CaL} , g_{K1} or g_{Kr} and keeping the others fixed at 100% of their original value.

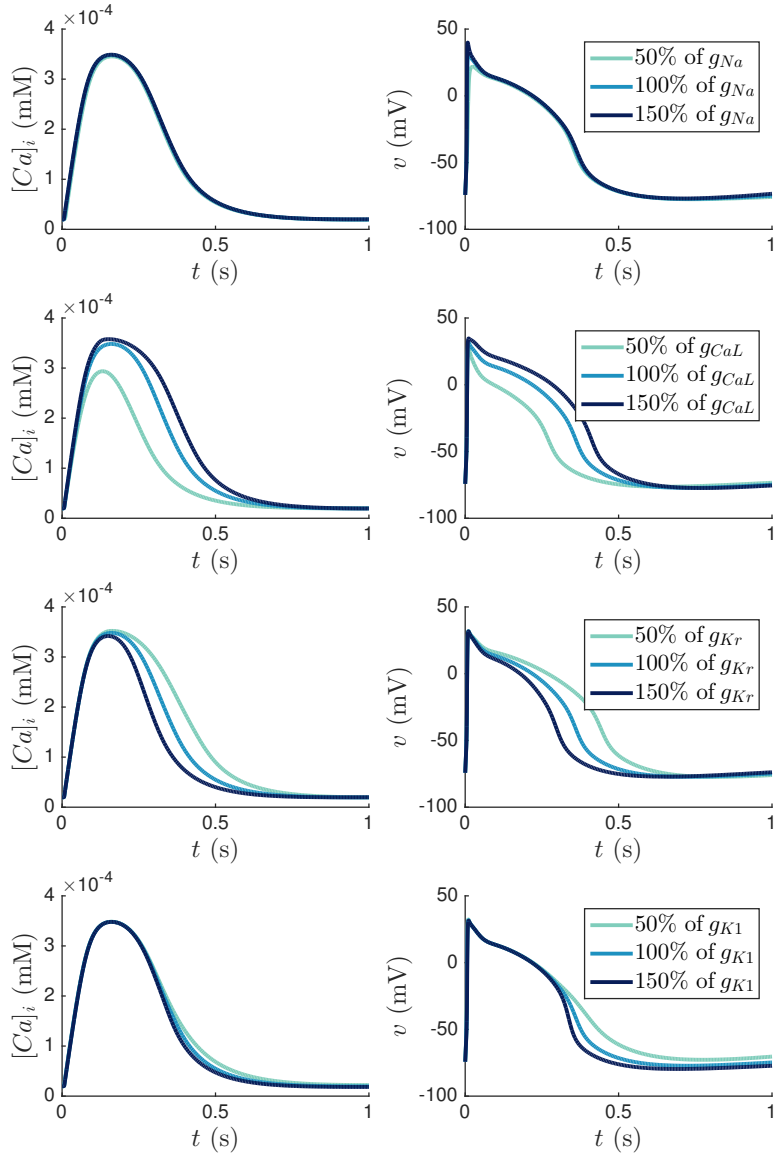


Figure 2: Single cell computations: plots of $[Ca]_i$ and v against t , for different parameter values. Single cell measurements.

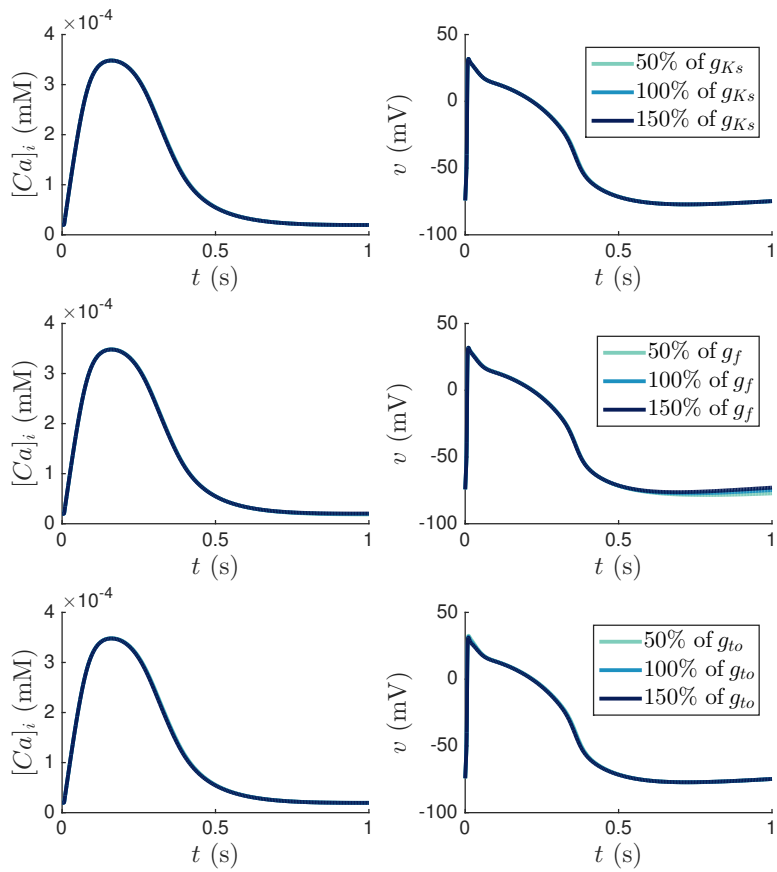


Figure 3: Single cell computations: plots of $[Ca]_i$ and v against t , for different parameter values.

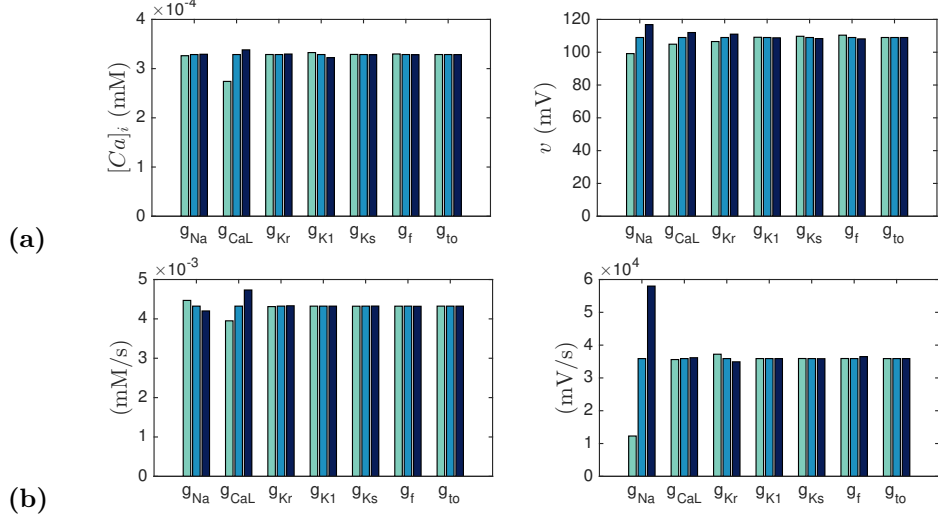


Figure 4: Single cell computations: the amplitude (a) and the maximum upstroke velocity V_{\max} (b) of $[Ca]_i$ (left) and v (right). Colour values are as in Figures 2 and 3. Single cell measurements.

Note that our observed data is obtained with all parameters at 100% of their original value. In Figure 11, we plot the left part of $\mathcal{J}_{\text{single cell}}$, the right part of $\mathcal{J}_{\text{single cell}}$, and its total value for different parameter values. By left and right part, we mean the contributions of $[Ca]_i$ and v to the size of $\mathcal{J}_{\text{single cell}}$ respectively. In Figure 12, we similarly plot the left part, the right part and the total value of \mathcal{J} . In Figure 16, we plot heat maps of the value of \mathcal{J} while varying two parameters at a time. When varying more than two parameters simultaneously, it becomes harder to visualise the results. However, we did vary all four parameters from 90% to 110% of their original value in steps of 2%. We computed the value of \mathcal{J} for all $11^4 = 14641$ points in this parameter space and found a unique local minimum when all four parameters are equal to their original values. Here, we define a local minimum as an element in our four dimensional matrix that is surrounded in all eight directions by larger valued elements. We will interpret our results in the discussion.

3.3.1 Alternative functionals

We define some alternative functionals: $\mathcal{J}_{\text{wave speed}}$, $\mathcal{J}_{\text{amplitude}} v$, $\mathcal{J}_{\text{amplitude}} [Ca]_i$, $\mathcal{J}_v 30\%$, $\mathcal{J}_{[Ca]_i} 30\%$, $\mathcal{J}_v 50\%$, $\mathcal{J}_{[Ca]_i} 50\%$, $\mathcal{J}_v 70\%$, $\mathcal{J}_{[Ca]_i} 70\%$, $\mathcal{J}_v 90\%$, and $\mathcal{J}_{[Ca]_i} 90\%$, where the names of the functionals refer to the characteristics as already mentioned in Subsections 3.1 and 3.2. We define $\mathcal{J}_{\text{wavespeed}}$ as the scaled difference in conductance velocity V_C between the observed and simulated data:

$$\mathcal{J}_{\text{wavespeed}} = \frac{\|V_C - V_{C \text{ obs}}\|^2}{\|V_{C \text{ obs}}\|^2}, \quad (10)$$

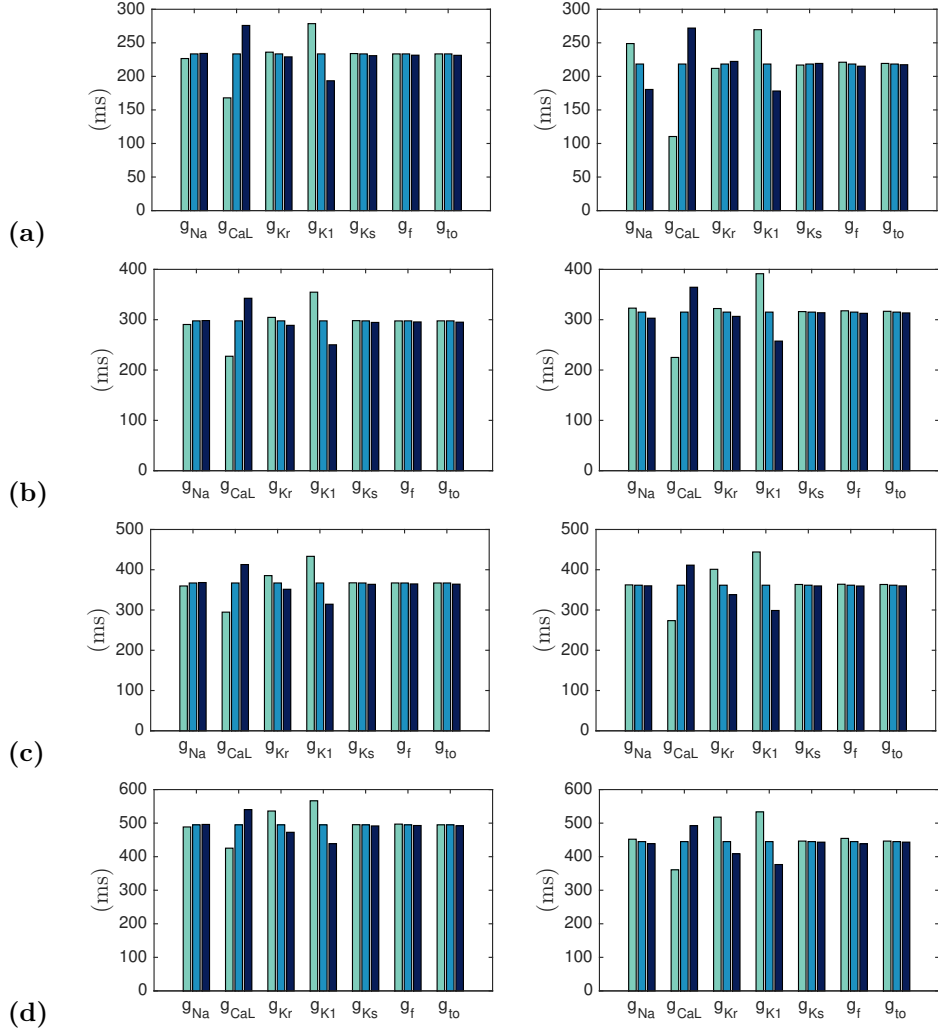


Figure 5: Single cell computations: the time the measured $[Ca]_i$ (left) or v (right) was above 30% (a), 50% (b), 70% (c), and 90% (d) of its amplitude. Colour values are as in Figures 2 and 3. Single cell measurements.

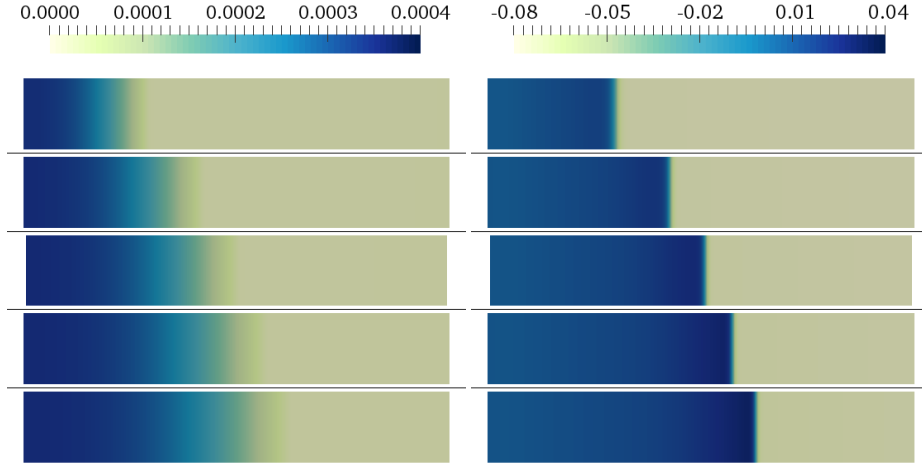


Figure 6: Heat maps of $[Ca]_i$ in μM (left), and v in V (right) of our 12 mm by 0.01 mm domain with, from top to bottom, g_{Na} at 50%, 75%, 100%, 125% and 150% of its default value. To increase visibility, we scaled the vertical axis of our 12 mm by 0.01 mm domain with a factor of 200.

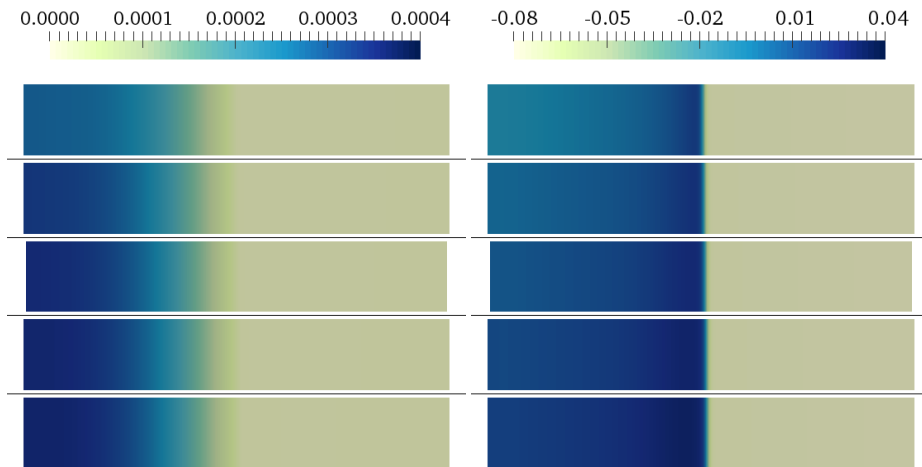


Figure 7: Heat maps of $[Ca]_i$ in μM (left), and v in V (right) of our 12 mm by 0.01 mm domain with, from top to bottom, g_{CaL} at 50%, 75%, 100%, 125% and 150% of its default value. To increase visibility, we scaled the vertical axis of our 12 mm by 0.01 mm domain with a factor of 200.

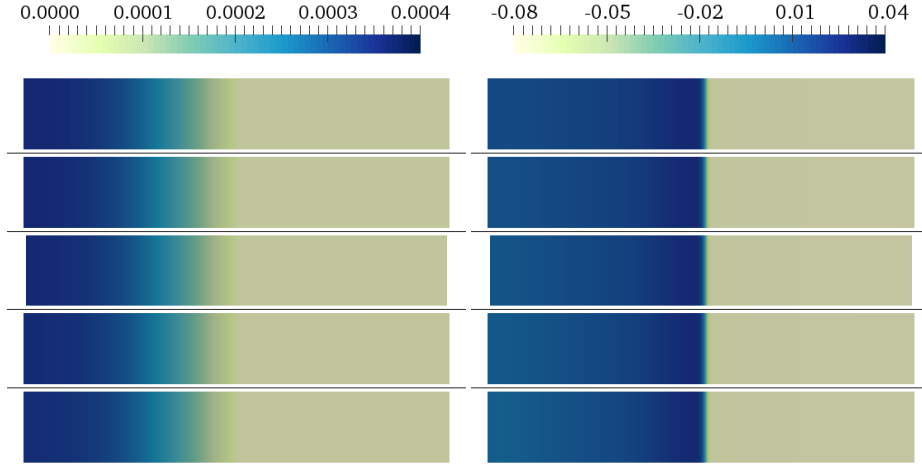


Figure 8: Heat maps of $[Ca]_i$ in μM (left), and v in V (right) of our 12 mm by 0.01 mm domain with, from top to bottom, g_{Kr} at 50%, 75%, 100%, 125% and 150% of its default value. To increase visibility, we scaled the vertical axis of our 12 mm by 0.01 mm domain with a factor of 200.

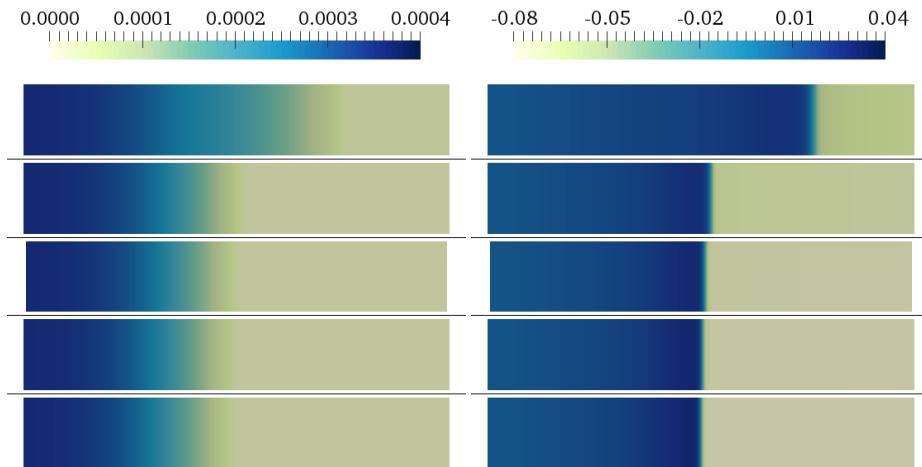


Figure 9: Heat maps of $[Ca]_i$ in μM (left), and v in V (right) of our 12 mm by 0.01 mm domain with, from top to bottom, g_{K1} at 50%, 75%, 100%, 125% and 150% of its default value. To increase visibility, we scaled the vertical axis of our 12 mm by 0.01 mm domain with a factor of 200.

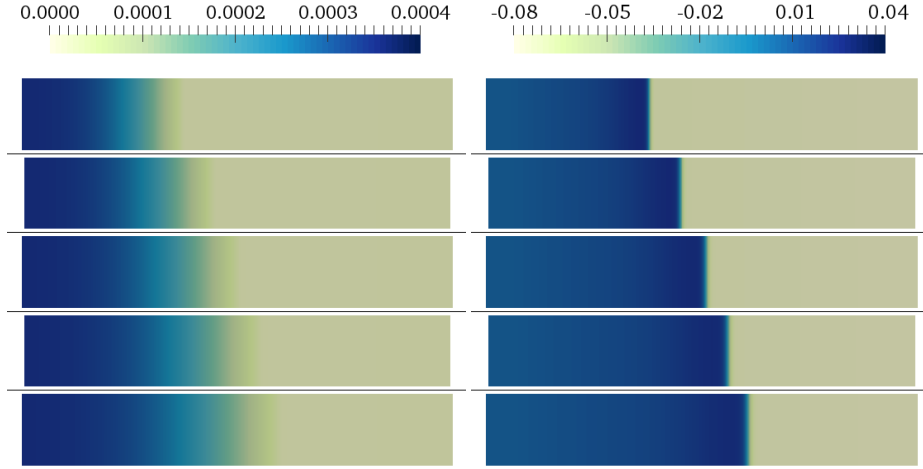


Figure 10: Heat maps of $[Ca]_i$ in μM (left), and v in V (right) of our 12 mm by 0.01 mm domain with, from top to bottom, σ_t at 50%, 75%, 100%, 125% and 150% of its default value. To increase visibility, we scaled the vertical axis of our 12 mm by 0.01 mm domain with a factor of 200.

For the other functionals, we calculated the average calcium and voltage wave, after time-shifting the data from every point in space so that all voltage peaks were overlapping. We then calculated the scaled difference between the observed and simulated data for that particular characteristic. In Figures 13, 14 and 15, we plot the values of the functionals for different parameter values. Note that we did not define a functional for the upstroke velocity, a characteristic that we did calculate before. We did not include such a functional, because we assume that the time resolution of our measurements is not high enough to accurately determine the upstroke velocity of the measured voltage and calcium waves.

3.3.2 Blocking

With the use of current blocker drugs, it is possible to (partially or fully) block ion channels of a specific type. In [15], the effect of several current blockers on their Paci2013 cell model was tested. In particular, they simulated the effect of Tetrodotoxin, an I_{Na} blocker, E4031, an I_{Kr} blocker, Nifedipine, an I_{CaL} blocker, and 3R4S-Chromanol 293B, an I_{Ks} blocker. These were the same blockers as were tested on the real iPSC-CMs by [14]. As an example, we simulate the full block of I_{Kr} , by setting g_{Kr} to zero. In Figure 17, we show the resulting $[Ca]_i$ and v wave.

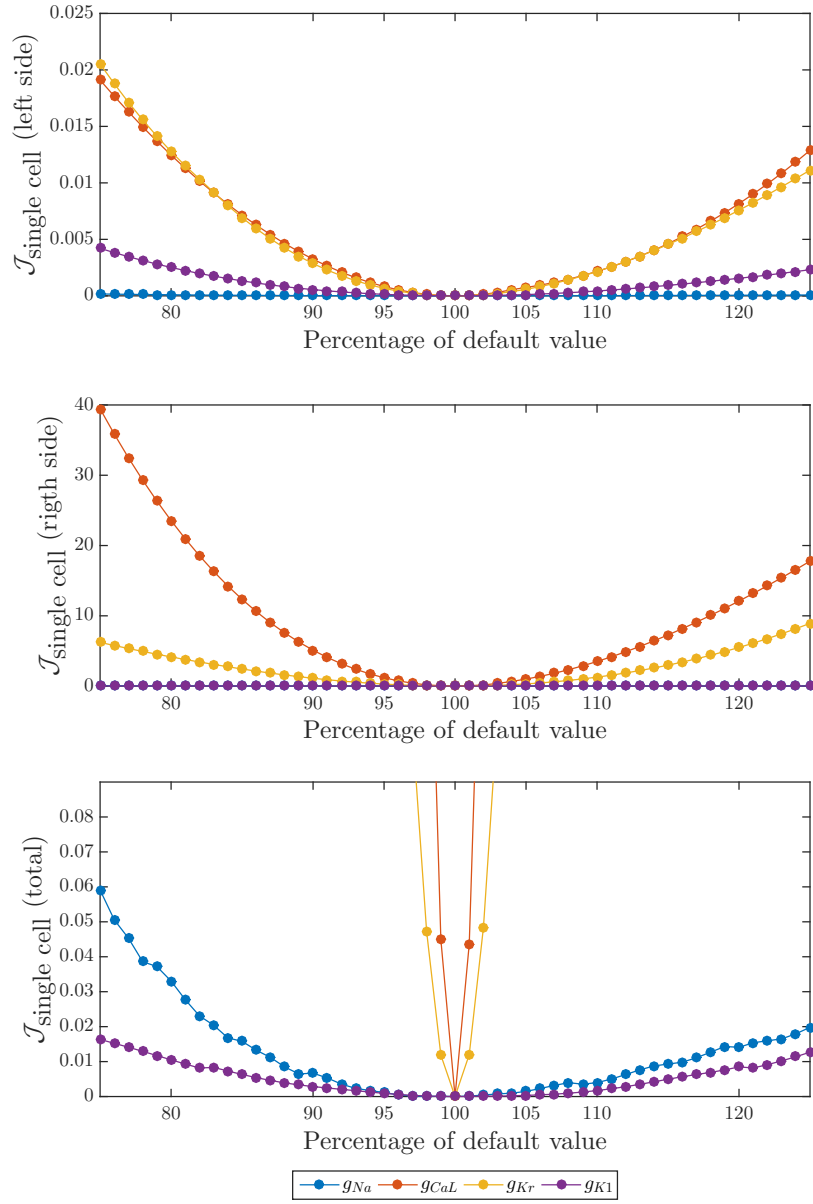


Figure 11: Single cell computations: the value of the part of $\mathcal{J}_{\text{single cell}}$ at the left side of the plus-sign (top), at the right side of the plus-sign (middle), and the total value of $\mathcal{J}_{\text{single cell}}$ (bottom), for varying percentages of the default parameter values.

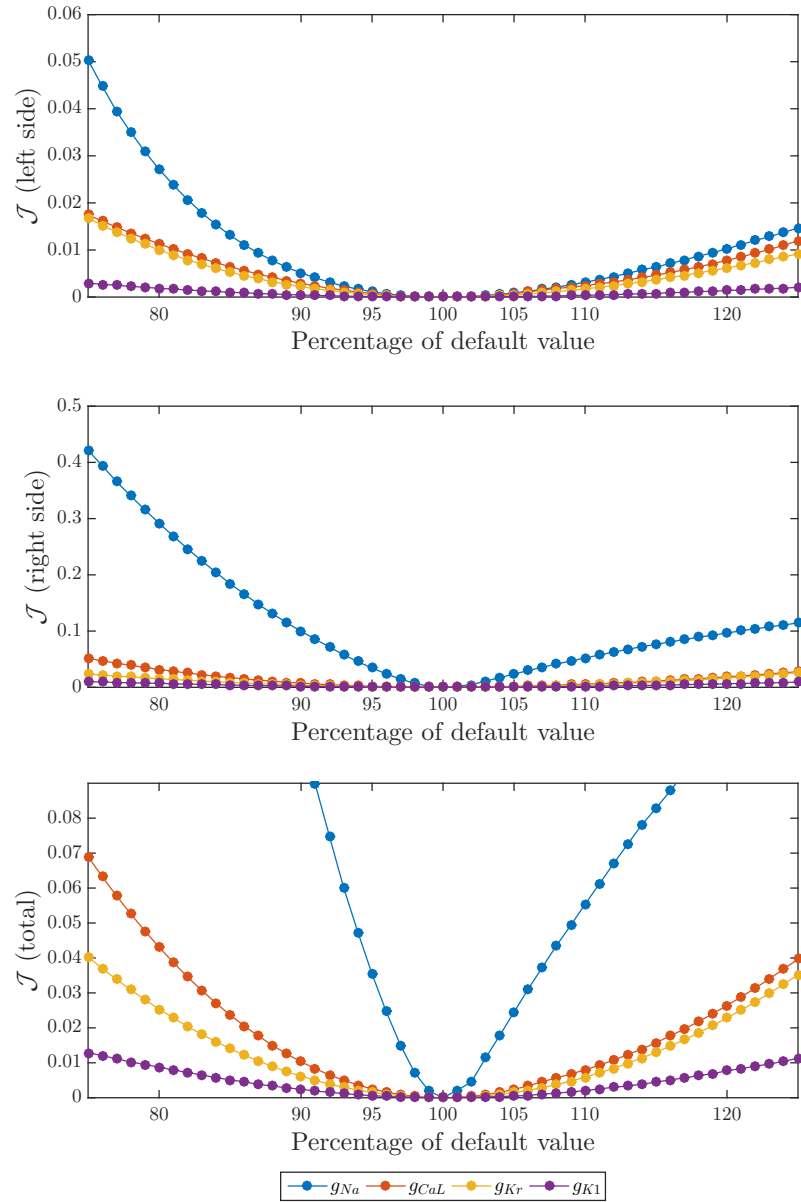


Figure 12: Tissue computations: the value of the part of \mathcal{J} at the left side of the plus-sign (top), at the right side of the plus-sign (middle), and the total value of \mathcal{J} (bottom), for varying percentages of the default parameter values.

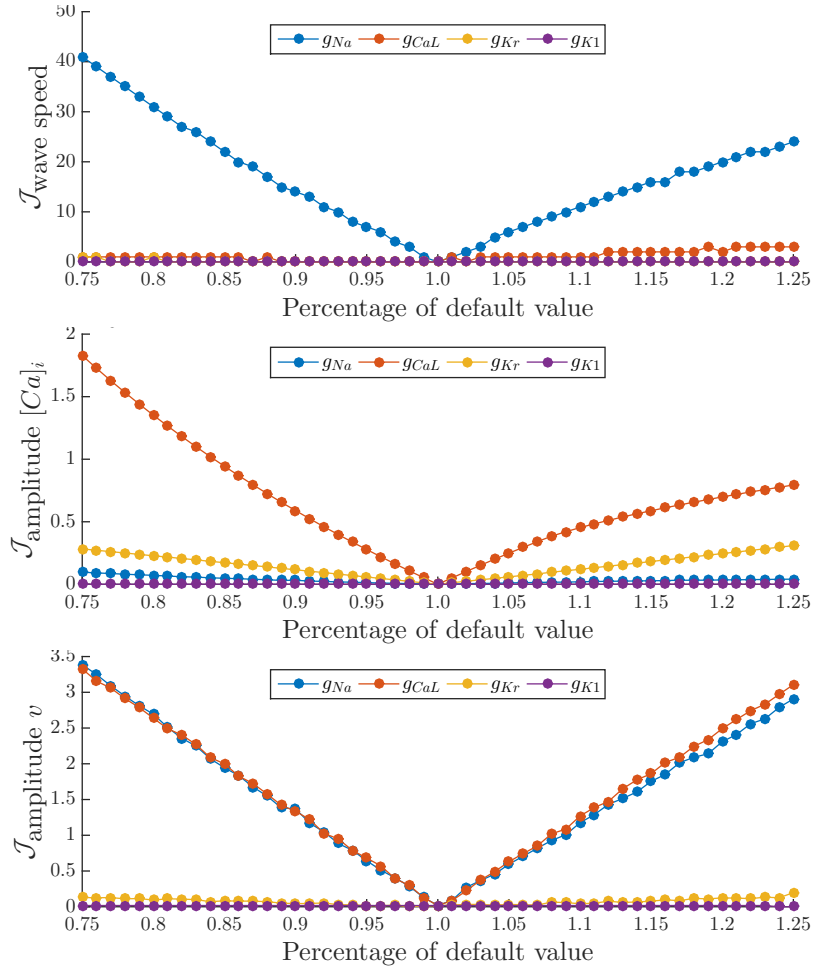


Figure 13: Tissue computations: the value of the part of several functionals, for varying percentages of the default parameter values.

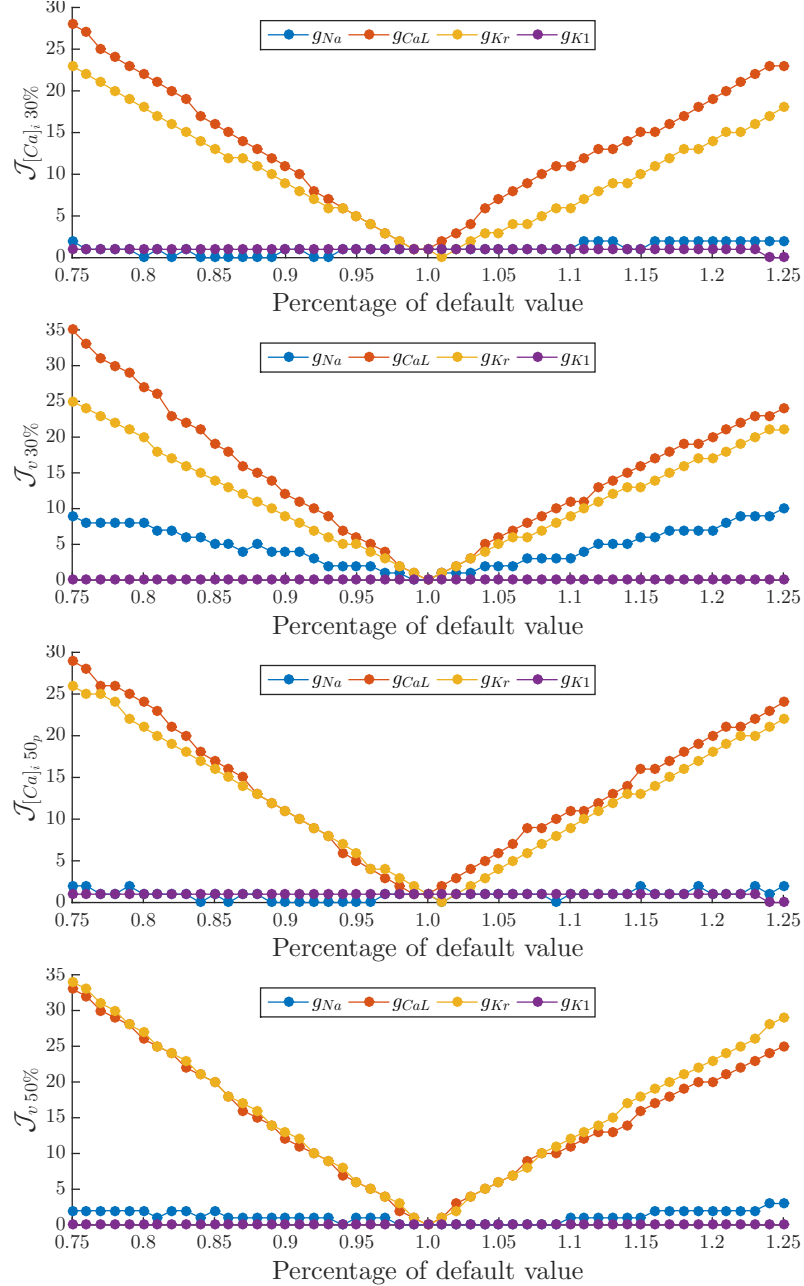


Figure 14: Tissue computations: the value of the part of several functionals, for varying percentages of the default parameter values.

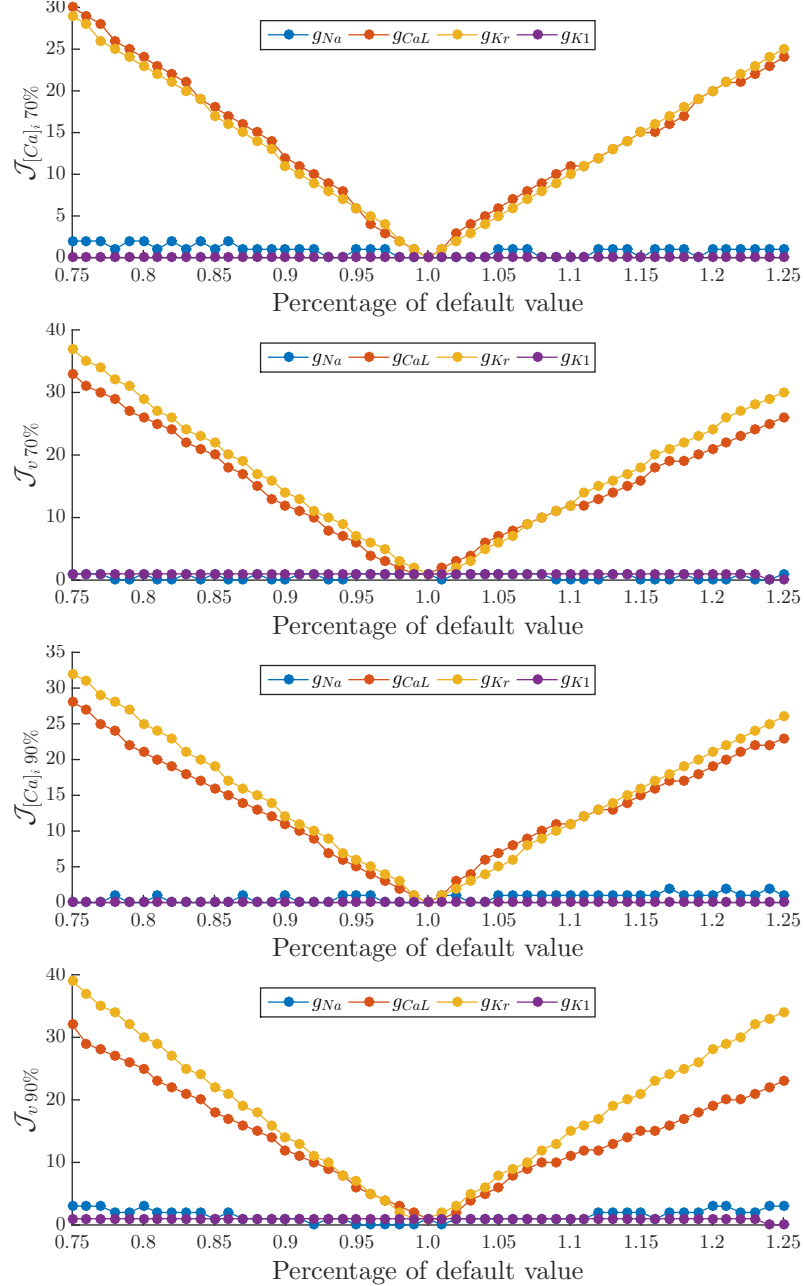


Figure 15: Tissue computations: the value of the part of several functionals, for varying percentages of the default parameter values.

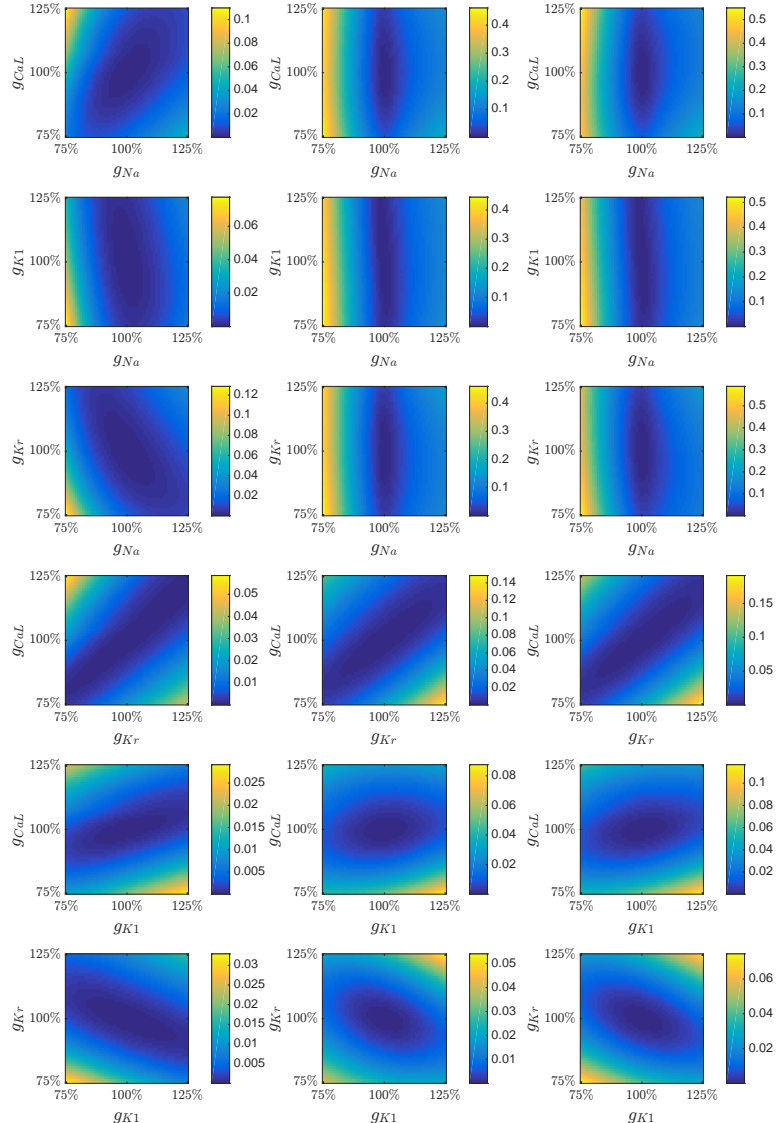


Figure 16: Tissue computations: the value of the part of \mathcal{J} at the left side of the plus-sign (left), at the right side of the plus-sign (middle), and the total value of \mathcal{J} (right), for varying percentages of the default parameter values.

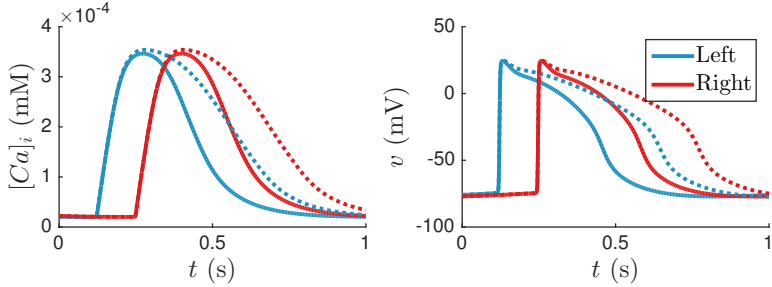


Figure 17: Plot of $[Ca]_i$ and v against t , at the left of the domain (in blue, at (5 mm, 0 mm)), at the right of the domain (in red, at (10 mm, 0 mm)), both with default parameter values (solid lines) and with fully blocked I_{Kr} (dotted lines).

| | \mathcal{J} | g_{Na} | \mathcal{J} | g_{Na} |
|---------------|-----------------------|----------|-----------------------|----------|
| Initial guess | | 90.000% | | 110.000% |
| Iteration 0 | 1.01×10^{-1} | 90.200% | 5.41×10^{-2} | 109.800% |
| Iteration 1 | 4.51×10^{-7} | 100.001% | 4.68×10^{-7} | 100.000% |
| Iteration 2 | 3.73×10^{-7} | 100.000% | 1.46×10^{-7} | 100.000% |

Table 1: The values of \mathcal{J} and g_{Na} at the start of each iteration of the IPOPT algorithm. We used two different initial values: $g_{Na} = 90\%$ (left), and $g_{Na} = 110\%$ (right).

3.3.3 Adjoint

To find a minimum of our functional \mathcal{J} , we use an adjoint-based approach.² Using cbcbeat and the dolfin-adjoint software on which it is based, we can automatically compute the total derivative of \mathcal{J} with respect to the different optimization parameters. We can then use the IPOPT optimisation algorithm [27] to find a minimum for our functional. At first, we only optimized for g_{Na} , the parameter to which our functional was most sensitive, see Figure 12. We assume that g_{Na} is bounded between 90% and 110% of its original value. We tried two different initial values: $g_{Na} = 90\%$ and $g_{Na} = 110\%$. In Table 1, the value of \mathcal{J} and the percentage of g_{Na} at the start of each iteration can be found. We see that the algorithm quickly converges to the true value of g_{Na} .

We can also optimize for more parameters at a time. As an example, we optimized for g_{Na} , g_{CaL} , g_{Kr} and g_{K1} , where all four parameters were bounded again between 90% and 110% of their original values. We took $g_{Na} = 90\%$, $g_{CaL} = 110\%$, $g_{Kr} = 90\%$ and $g_{K1} = 110\%$ as initial guess. The results can be found in Table 2.

²See, for example, [9] for an introductory text in adjoint-based optimization methods.

| | \mathcal{J} | g_{Na} | g_{CaL} | g_{Kr} | g_{K1} |
|---------------|-----------------------|-----------------|------------------|-----------------|-----------------|
| Initial guess | | 90.000% | 110.000% | 90.000% | 110.000% |
| Iteration 0 | 1.07×10^{-1} | 90.200% | 109.800% | 90.200% | 109.800% |
| Iteration 1 | 5.88×10^{-2} | 109.802% | 90.646% | 109.271% | 90.629% |
| Iteration 2 | 1.14×10^{-2} | 102.882% | 97.306% | 102.660% | 97.300% |
| Iteration 3 | 1.65×10^{-3} | 99.026% | 99.881% | 100.299% | 99.904% |
| Iteration 4 | 3.73×10^{-4} | 99.537% | 99.893% | 100.202% | 99.903% |
| Iteration 5 | 4.57×10^{-6} | 100.047% | 99.923% | 100.083% | 99.919% |
| Iteration 6 | 9.75×10^{-7} | 100.000% | 99.925% | 100.089% | 99.922% |

Table 2: The values of \mathcal{J} , g_{Na} , g_{CaL} , g_{Kr} and g_{K1} at the start of each iteration of the IPOPT algorithm. We took $g_{\text{Na}} = 90\%$ and $g_{\text{CaL}} = 110\%$ and $g_{\text{K1}} = 90\%$ and $g_{\text{Kr}} = 110\%$ as initial guess.

4 Discussion

4.1 Sensitivity

In Figure 18, the main ion currents that are responsible for the ventricular action potential are shown. In the bottom right corner, we indicate four action potential phases: **(0)**, **(1)**, **(2)**, and **(3)**. The action potential starts with a rapid depolarization due to sodium ion influx **(0)**, followed by a fast repolarization due to potassium ion outflux **(1)**, a plateau phase, where the repolarization is slowed down due to calcium ion influx **(2)**, and a final repolarization phase, due to further postassium ion outflux **(3)**. All these currents are the result of the opening and closing of different types of ion channels in the cell membrane. We also measure the intracellular calcium concentration, that rises as a result of the release of a large amount of calcium ions into the cytoplasm by the sarcoplasmic reticulum, a calcium ion store inside the cell. The release of calcium ions by the sarcoplasmic reticulum is triggered by the influx of calcium ions due to the opening of calcium ion channels in the cell membrane during the action potential. This process is called calcium induced calcium release [10].

We will now interpret Figures 2–5, where we showed plots of the intracellular calcium concentration and potential for different parameter values and several characteristics of our measurements. When g_{Na} decreases, the maximum voltage decreases as well. This is as expected, because the influx of sodium ions due to the opening of sodium channels causes a depolarization peak, see Figure 18, top left. When less channels open, I_{Na} will be less strong and the voltage peak will be smaller. The intracellular calcium curve is not affected. When g_{CaL} decreases, the initial voltage peak decreases and the voltage is lower during the plateau phase. As I_{CaL} causes a delay of the repolarization, see Figure 18, top right, this is as expected. We also see an increase of the intracellular calcium concentration curve when g_{CaL} is increased: we recognise the calcium induced calcium release. Decreasing g_{Kr} and g_{K1} prolongs the repolarization of the cell membrane, as the potassium ion outflux is responsible for the process, see the

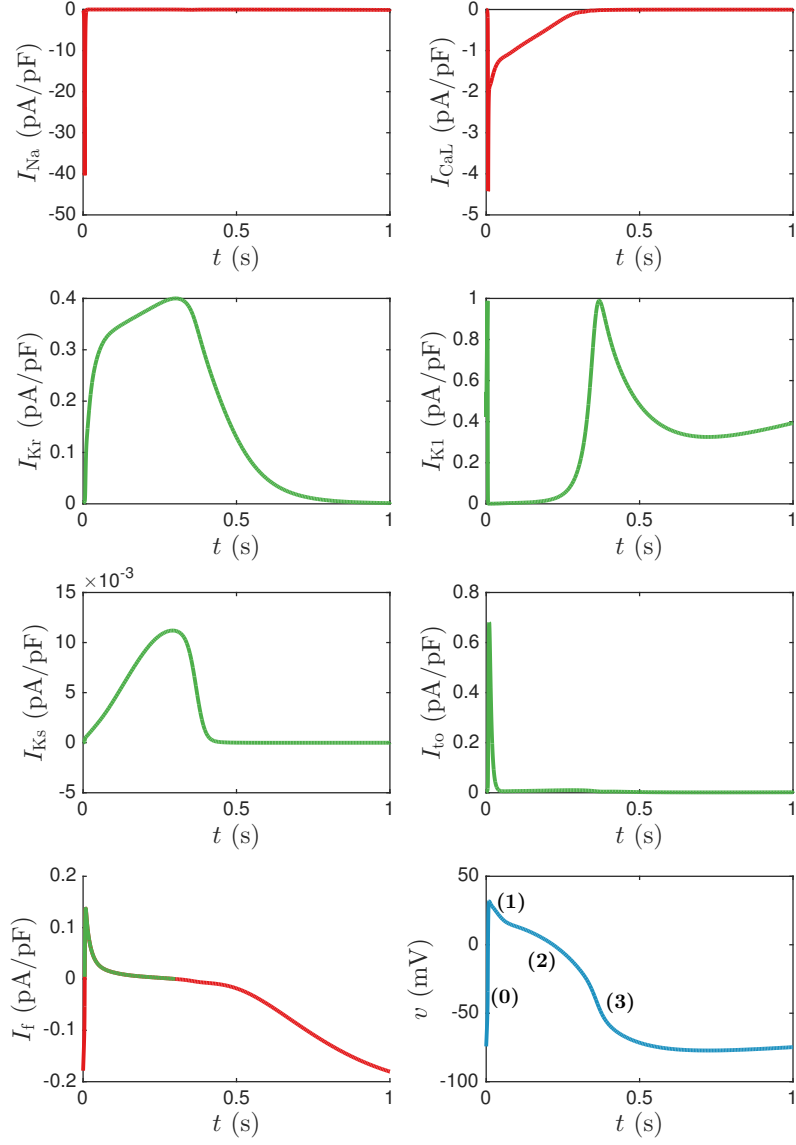


Figure 18: Plots of the ionic currents $I_{\text{Na}}, I_{\text{CaL}}, I_{\text{Kr}}, I_{\text{K1}}, I_{\text{Ks}}, I_{\text{to}}$ and I_f against t . Inward, depolarizing currents in red and outward, repolarizing currents in green. In the bottom right corner, we indicate four action potential phases: the rapid depolarization due to sodium ion influx **(0)**, the fast repolarization due to potassium ion outflux **(1)**, the plateau phase, where the repolarization is slowed down due to calcium ion influx **(2)**, and the final repolarization phase **(3)**, due to further postpotassium ion outflux. Single cell measurements.

corresponding currents in Figure 18. We also see that the intracellular calcium concentration decreases more slowly in these cases. We see that decreasing g_{K1} has mainly effect at the end of the repolarization phase (phase (3)), whereas decreasing g_K mainly prolongs the plateau phase (2). Finally, we see that varying g_{Ks} , g_f or g_{to} has almost no visible effect on our measurements. We see that the peak of I_{Ks} is very small, see Figure 18. The peak of the outward I_{to} and the outward part of I_f are larger, but both currents peak at a moment that the much larger inward I_{Na} and I_{CaL} are at their peak as well. We do see some small effect of I_f on the final part of our voltage measurements. Note that varying g_{Ks} , g_f or g_{to} might very well have an effect on our measurements when a different stimulation protocol is used. However, we will not investigate this further and will assume those parameters are fixed from now on.

For our tissue computations, the same observations as for the single cell computations hold. We see that varying σ_t does mainly affect the conductance velocity, see Figures 21 and 22. The conductance velocity is further affected by g_{Na} . We also observe that setting g_{K1} to 50% of its original value results in a highly increased conductance velocity. However, when we look at Figure 19, we see that in this case the voltage does increase from the start (turquoise and orange lines), before the wave even reaches these points. This is the reason for the observed peak in conductance velocity. When we look at the range of 75% to 125% of the original value of g_{K1} , we do not observe any change in conductance velocity, see Figure 9. Therefore, we will assume that the conductance velocity is not affected by g_{K1} .

4.2 Inversion

When we look at Figure 12, we see that \mathcal{J} is mainly sensitive to g_{Na} . This is the case because our functional is mainly sensitive to changes in the wave speed, i.e. conductance velocity, which the other three parameters barely affect when we look at a range of 75% to 125% of their original values, see Figures 6 and 7. Conversely, $\mathcal{J}_{\text{single cell}}$ is insensitive to changes in g_{Na} , but is very sensitive to changes in g_{CaL} and g_{Kr} , see Figure 11. This, again, is as expected when we look back at Figure 2: varying g_{CaL} or g_{Kr} affects the shape of the waves more than varying g_{Na} or g_{K1} .

We also defined some alternative functionals, to show more clearly that different characteristics of our data are differently affected by the four different parameters we examined. For example, as said before, the wave speed is mainly affected by g_{Na} . Therefore, $\mathcal{J}_{\text{wave speed}}$ is mainly sensitive to g_{Na} , see Figure 13 (top). We observe too that by spatially averaging our measured data, as we did to calculate the alternative functionals, we would decrease the level of noise and diversity of real measured data. By removing the spatial element from the data in this way, we could also use our single cell functional on our averaged data. Especially when we are interested in parameters such as g_{CaL} , g_{K1} , g_{Kr} , that do barely affect the wave speed, but do affect the shape of the waves, this could be useful.

Further, we mentioned blocking as a possible way to reduce the number

of ion channel currents and thereby also the number of parameters involved. Blocking can be used as well to study the effect of one particular ion channel, by measuring the voltage and calcium waves before and after blocking this channel type completely.

Finally, we looked briefly at an optimization algorithm and how this could be used to find a minimum of our functional \mathcal{J} . We optimized both for the g_{Na} parameter alone and for the four parameters g_{Na} , g_{CaL} , g_{K1} and g_{Kr} simultaneously. We see that the IPOPT algorithm quickly converges, see Tables 1 and 2.

4.3 Conclusion

The classic technique to estimate electro-physiological cardiac parameters is patch clamping, with which the transmembrane voltage of a single cell can be precisely measured over time. Using blocking and many different stimulation protocols, it is possible to determine the different cardiac parameters of a cell. An alternative for the time and labour intensive patch clamping technique could be optical mapping, with which voltage and calcium waves of a cluster of cells can be measured simultaneously. Although optical mapping techniques do not produce action potential measurements that are equivalent to the golden standard patch clamping measurements, they do add a spatial dimension to the measurements: with optical mapping, we can measure the wave speed/conductance velocity of the action potential. On top of that, optical mapping records not only voltage, but also calcium waves. These advantages might outweigh the disadvantage of inaccuracy of the method. In this report, we mainly considered the conductance parameters of the fast sodium current I_{Na} , the L-type calcium current I_{CaL} , the inward rectifier current I_{K1} and the rapid delayed rectifier current I_{Kr} . We defined cost functionals \mathcal{J} and found unique minima for those four parameters. Of course, there are many more parameters that shape the measured voltage and calcium waves, some of them more important than others. With different stimulation protocols - we only considered one - and the use of different drugs to block certain channels, it might be possible to uniquely determine their values. There are many other factors that we should take into consideration. The range over which parameters vary might be very diverse. Our measurements will be more sensitive to some parameters than others. We could be particularly interested in the abnormal value of a certain parameter, for instance because it is the indicator of a particular disease. Similarly, there could be parameters that we are not that interested in and stimulation protocols could be designed that are insensitive to those parameters. Further, we should take into account measurement errors and noise. The distribution of ion channels in the cells of a monolayer might vary considerably between different cells. Therefore, when optimizing, we could also look at spatially dependent parameters, with different values for every cell. Finally, we could look at other mathematical models than the monodomain equations and Paci2013 cell model that we used. In conclusion, inversion based on optical mapping observations looks promising and when both optical mapping recording techniques

and iPSC-CM monolayer production become more mature, might become used in the future.

References

- [1] SATISH BALAY, SHRIRANG ABHYANKAR, MARK F ADAMS, JED BROWN, PETER BRUNE, KRIS BUSCHELMAN, LISANDRO DALCIN, VICTOR EIJKHOUT, WILLIAM D GROPP, DINESH KAUSHIK, MATTHEW G KNEPLEY, LOIS CURFMAN MCINNES, KARL RUPP, BARRY F SMITH, STEFANO ZAMPINI, HONG ZHANG, AND HONG ZHANG. PETSc users manual. Technical Report ANL-95/11 - Revision 3.7, Argonne National Laboratory, 2016.
- [2] SATISH BALAY, WILLIAM D GROPP, LOIS C MCINNES, AND BARRY F SMITH. Efficient management of parallelism in object oriented numerical software libraries. In ERLEND ARGE, ARE MAGNUS BRUASET, AND HANS PETTER LANGTANGEN, editors, *Modern Software Tools in Scientific Computing*, pages 163–202. Birkhäuser Press, 1997.
- [3] ROGER C BARR AND ROBERT PLONSEY. Propagation of excitation in idealized anisotropic two-dimensional tissue. *Biophysical Journal*, **45**(6):1191–1202, 1984.
- [4] ADRIANA BLAZESKI, RENJUN ZHU, DAVID W HUNTER, SETH H WEINBERG, KENNETH R BOHELER, ELIAS T ZAMBIDIS, AND LESLIE TUNG. Electrophysiological and contractile function of cardiomyocytes derived from human embryonic stem cells. *Progress in Biophysics and Molecular Biology*, **110**(2):178–195, 2012.
- [5] ZHIFEN CHEN, WENYING XIAN, MILENA BELLIN, TATJANA DORN, QINGHAI TIAN, ALEXANDER GOEDEL, LISA DREIZEHNTER, CHRISTINE M SCHNEIDER, DORIEN WARD-VAN OOSTWAARD, JUDY KING MAN NG, ET AL. Subtype-specific promoter-driven action potential imaging for precise disease modelling and drug testing in hpsc-derived cardiomyocytes. *European Heart Journal*, **38**(4):292–301, 2017.
- [6] GRAHAM T DEMPSEY, KHURAM W CHAUDHARY, NICHOLAS ATWATER, CUONG NGUYEN, BARRY S BROWN, JOHN D MCNEISH, ADAM E COHEN, AND JOEL M KRALJ. Cardiotoxicity screening with simultaneous optogenetic pacing, voltage imaging and calcium imaging. *Journal of Pharmacological and Toxicological Methods*, **81**:240–250, 2016.
- [7] CHRIS DENNING, VIOLA BORGDORFF, JAMES CRUTCHLEY, KARL SA FIRTH, VINOJ GEORGE, SPANDAN KALRA, ALEXANDER KONDRASHOV, MINH DUC HOANG, DIOGO MOSQUEIRA, ASHA PATEL, ET AL. Cardiomyocytes from human pluripotent stem cells: from laboratory curiosity to industrial biomedical platform. *Biochimica et Biophysica Acta (BBA)-Molecular Cell Research*, **1863**(7):1728–1748, 2016.

- [8] PATRICK E FARRELL, DAVID A HAM, SIMON W FUNKE, AND MARIE E ROGNES. Automated derivation of the adjoint of high-level transient finite element programs. *SIAM Journal on Scientific Computing*, **35**(4):C369–C393, 2013.
- [9] MAX D GUNZBURGER. *Perspectives in flow control and optimization*. SIAM, 2002.
- [10] JAMES P KEENER AND JAMES SNEYD. *Mathematical Physiology*. Springer, 2009.
- [11] PETER LEE, MATT KLOS, CHRISTIAN BOLLENSDORFF, LUQIA HOU, PAUL EWART, TIMOTHY J KAMP, JIANHUA ZHANG, ALEXANDRA BIZY, GUADALUPE GUERRERO-SERNA, PETER KOHL, ET AL. Simultaneous voltage and calcium mapping of genetically purified human induced pluripotent stem cell-derived cardiac myocyte monolayers. *Circulation Research*, **110**(12):1556–1563, 2012.
- [12] CATHERINE M LLOYD, JAMES R LAWSON, PETER J HUNTER, AND POUL F NIELSEN. The cellml model repository. *Bioinformatics*, **24**(18):2122–2123, 2008.
- [13] ANDERS LOGG, KENT-ANDRE MARDAL, AND GARTH WELLS. *Automated solution of differential equations by the finite element method: The FEniCS book*, **84**. Springer Science & Business Media, 2012.
- [14] JUNYI MA, LIANG GUO, STEVE J FIENE, BLAKE D ANSON, JAMES A THOMSON, TIMOTHY J KAMP, KYLE L KOLAJA, BRADLEY J SWANSON, AND CRAIG T JANUARY. High purity human-induced pluripotent stem cell-derived cardiomyocytes: Electrophysiological properties of action potentials and ionic currents. *American Journal of Physiology - Heart and Circulatory Physiology*, **301**(5):H2006–H2017, 2011.
- [15] MICHELANGELO PACI, JARI HYTTINEN, KATRIINA AALTO-SETÄLÄ, AND STEFANO SEVERI. Computational models of ventricular-and atrial-like human induced pluripotent stem cell derived cardiomyocytes. *Annals of Biomedical Engineering*, **41**(11):2334–2348, 2013.
- [16] MICHELANGELO PACI, JARI HYTTINEN, BLANCA RODRIGUEZ, AND STEFANO SEVERI. Human induced pluripotent stem cell-derived versus adult cardiomyocytes: an *in silico* electrophysiological study on effects of ionic current block. *British Journal of Pharmacology*, **172**(21):5147–5160, 2015.
- [17] ROBERT PLONSEY AND ROGER BARR. The four-electrode resistivity technique as applied to cardiac muscle. *IEEE Transactions on Biomedical Engineering*, **29**(7):541–546, 1982.
- [18] DIVYA RAJAMOHAN, ELENA MATSA, SPANDAN KALRA, JAMES CRUTCHLEY, ASHA PATEL, VINOJ GEORGE, AND CHRIS DENNING. Current status

- of drug screening and disease modelling in human pluripotent stem cells. *Bioessays*, **35**(3):281–298, 2013.
- [19] MARIE E ROGNES, PATRICK E FARRELL, SIMON W FUNKE, JOHAN E HAKE, AND MOLLY MALECKAR. Cbcbeat: an adjoint-enabled framework for computational cardiac electrophysiology. *Journal of Open Source Software*, 06/2017 2017.
 - [20] BERT SAKMANN. *Single-channel recording*. Springer Science & Business Media, 2013.
 - [21] LUCA SALA, MILENA BELLIN, AND CHRISTINE L MUMMERY. Integrating cardiomyocytes from human pluripotent stem cells in safety pharmacology: has the time come? *British Journal of Pharmacology*. <http://dx.doi.org/10.1111/bph.13577> [Epub], 2016.
 - [22] NESTOR G SEPULVEDA, BRADLEY J ROTH, AND JOHN P WIJKSWO. Current injection into a two-dimensional anisotropic bidomain. *Biophysical Journal*, **55**(5):987–999, 1989.
 - [23] PRAVEEN SHUKLA AND JOSEPH C WU. Cardiac subtype characterization using all-optical action potential imaging. *European Heart Journal*, **38**(4):302, 2017.
 - [24] JOAKIM SUNDNES, ROBERT ARTEBRANT, OLA SKAVHAUG, AND ASLAK TVEITO. A second-order algorithm for solving dynamic cell membrane equations. *IEEE Transactions on Biomedical Engineering*, **56**(10):2546–2548, Oct 2009.
 - [25] JOAKIM SUNDNES, BJØRN FREDRIK NIELSEN, KENT ANDRE MARDAL, XING CAI, GLENN TERJE LINES, AND ASLAK TVEITO. On the computational complexity of the bidomain and the monodomain models of electrophysiology. *Annals of Biomedical Engineering*, **34**(7):1088–1097, 2006.
 - [26] KAZUTOSHI TAKAHASHI, KOJI TANABE, MARI OHNUKI, MEGUMI NARITA, TOMOKO ICHISAKA, KIICHIRO TOMODA, AND SHINYA YAMANAKA. Induction of pluripotent stem cells from adult human fibroblasts by defined factors. *Cell*, **131**(5):861–872, 2007.
 - [27] ANDREAS WÄCHTER AND LORENZ T BIEGLER. On the implementation of an interior-point filter line-search algorithm for large-scale nonlinear programming. *Mathematical programming*, **106**(1):25–57, 2006.
 - [28] RENJUN ZHU, MICHAL A MILLROD, ELIAS T ZAMBIDIS, AND LESLIE TUNG. Variability of action potentials within and among cardiac cell clusters derived from human embryonic stem cells. *Scientific Reports*, **6**, 2016.

Appendix

This Appendix contains Figures 19, 20, 21, and 22.

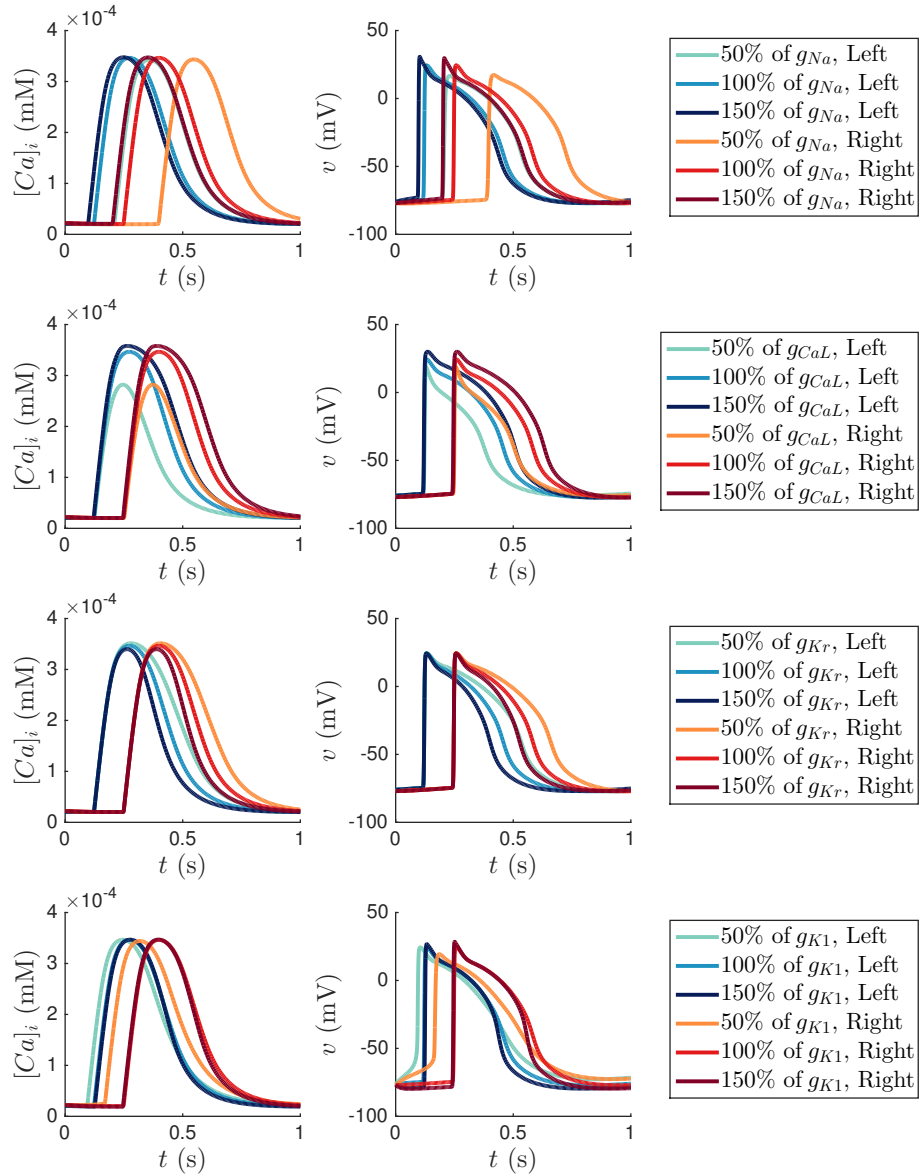


Figure 19: Tissue computations: plots of $[Ca]_i$ and v against t , at the left of the domain (in blue, at $(5 \text{ mm}, 0 \text{ mm})$) and at the right of the domain (in red, at $(10 \text{ mm}, 0 \text{ mm})$), for different parameter values. The total domain size is 12 mm by 0.01 mm.

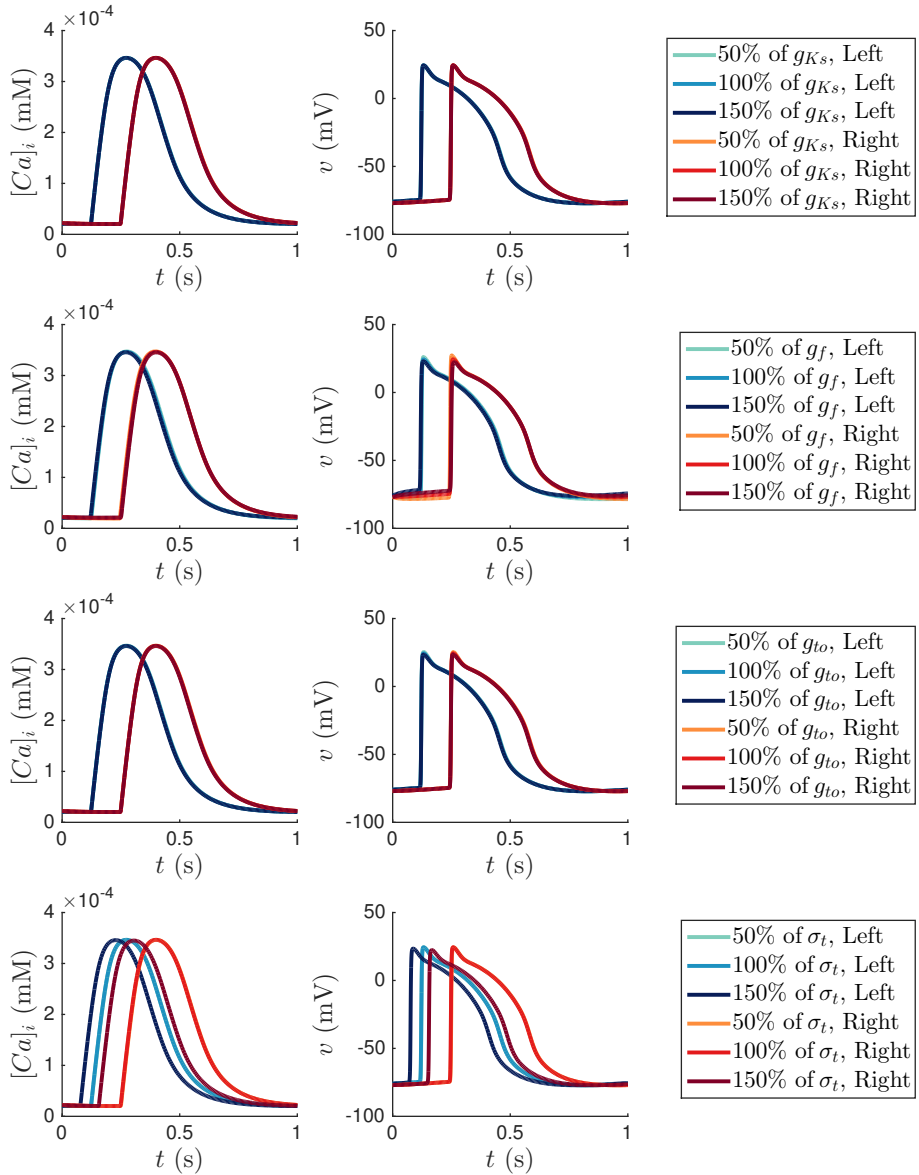


Figure 20: Tissue computations: plots of $[Ca]_i$ and v against t , at the left of the domain (in blue, at $(5 \text{ mm}, 0 \text{ mm})$) and at the right of the domain (in red, at $(10 \text{ mm}, 0 \text{ mm})$), for different parameter values. The total domain size is 12 mm by 0.01 mm.

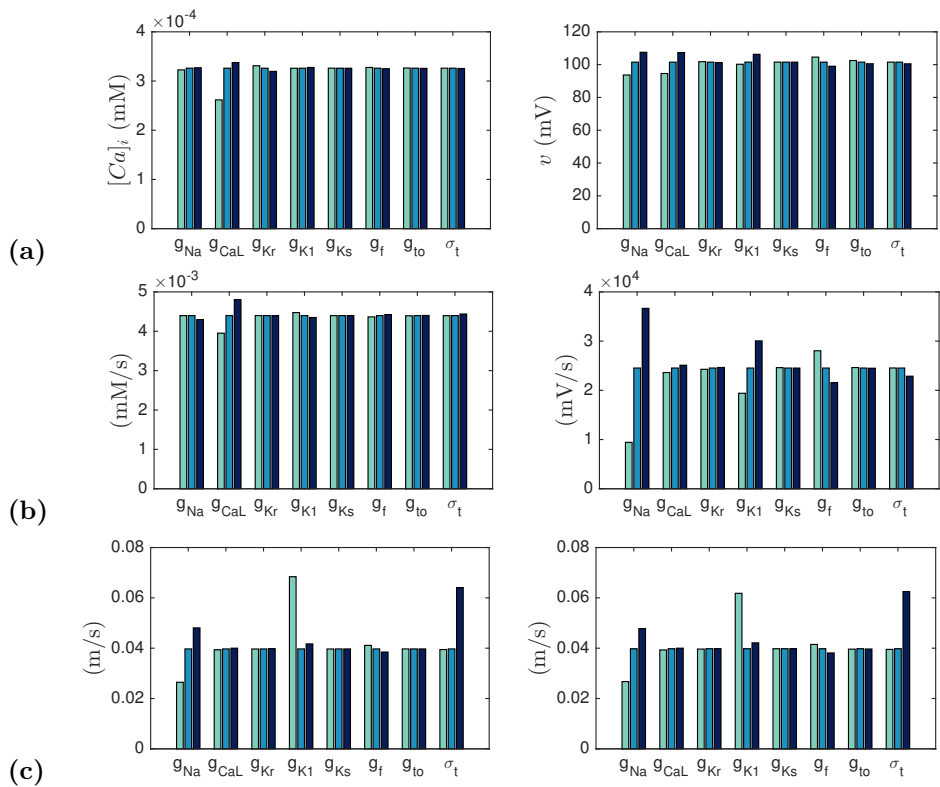


Figure 21: Tissue computations: the amplitude (a), maximum upstroke velocity V_{\max} (b) and conductance velocity V_C (c) of $[Ca]_i$ (left) and v (right). Colour values are as in Figures 19 and 20.

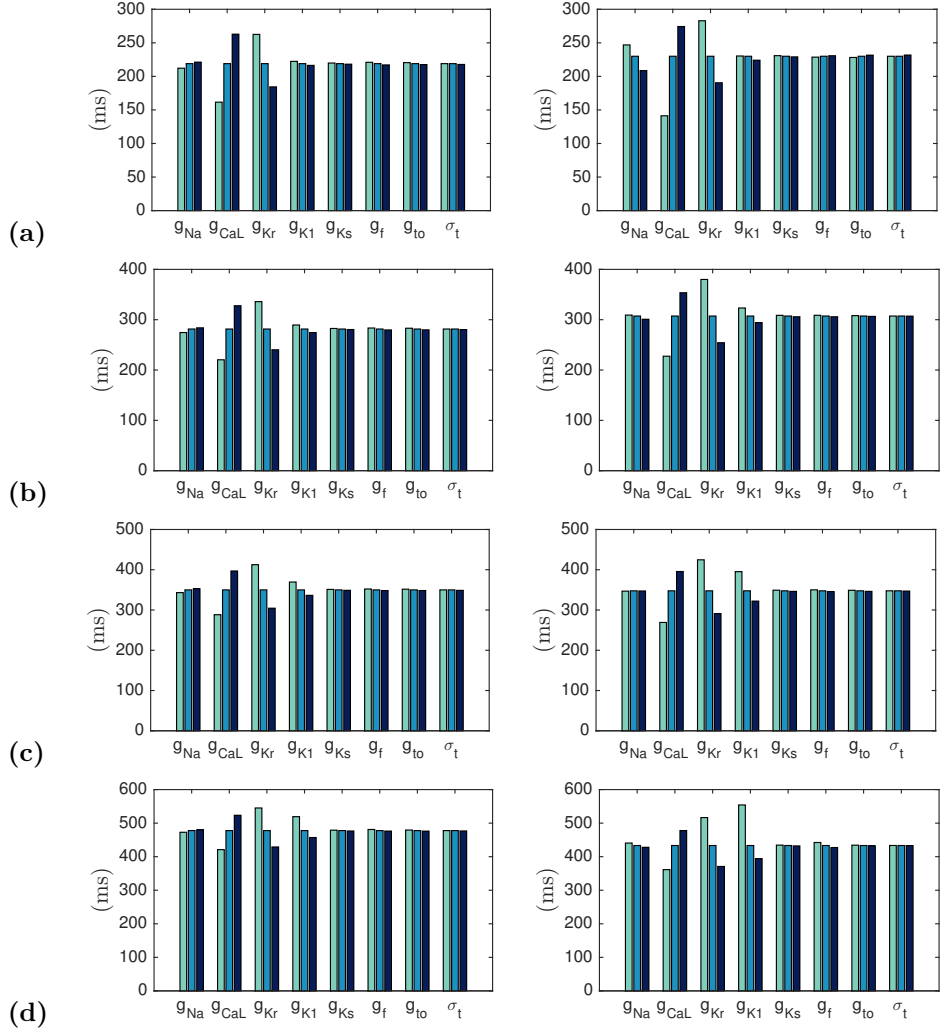


Figure 22: Tissue computations: the time the measured $[Ca]_i$ (left) or v (right) was above 30% (a), 50% (b), 70% (c), and 90% (d) of its amplitude. Colour values are as in Figures 19 and 20.